
DeepRV: pre-trained spatial priors for accelerated disease mapping.

Jhonathan Navott¹

Daniel Jenson²

Seth Flaxman²

Elizaveta Semenova¹

¹Department of Epidemiology and Biostatistics, Imperial College London, UK

²Department of Computer Science, University of Oxford, UK

Abstract

Recently introduced prior-encoding deep generative models (*e.g.*, PriorVAE, π VAE, and PriorCVAE) have emerged as powerful tools for scalable Bayesian inference by emulating complex stochastic processes like Gaussian processes (GPs). However, these methods remain largely a proof-of-concept and inaccessible to practitioners. We propose **DeepRV**, a lightweight, decoder-only approach that accelerates training, and enhances real-world applicability in comparison to current VAE-based prior encoding approaches. Leveraging probabilistic programming frameworks (*e.g.*, NumPyro) for inference, DeepRV achieves significant speedups while also improving the quality of parameter inference, closely matching full MCMC sampling. We showcase its effectiveness in process emulation and spatial analysis of the UK using simulated data, gender-wise cancer mortality rates for individuals under 50, and HIV prevalence in Zimbabwe. To bridge the gap between theory and practice, we provide a user-friendly API, enabling scalable and efficient Bayesian inference.

large datasets. Recent advances in deep generative models (DGMs) have introduced the concept of pre-training priors for Bayesian inference, offering a potential solution to these bottlenecks. Frameworks such as PriorVAE [Semenova et al., 2022], π VAE [Mishra et al., 2022], PriorCVAE [Semenova et al., 2023b], and aggVAE [Semenova et al., 2023a] have demonstrated the feasibility of encoding complex priors using DGMs, enabling faster inference by decoupling the computational burden of prior construction from the inference stage.

However, these methods remain largely a proof-of-concept and inaccessible to practitioners. They often require substantial expertise in deep learning model implementation, and their computational efficiency gains are offset by the complexity of training variational autoencoders (VAEs) [Kingma, 2013]. Further, VAEs are prone to *posterior collapse*, a phenomenon where the model effectively disregards a subset of the latent variables, thereby failing to capture meaningful variations in the data [Lucas et al., 2019, Wang et al., 2021]. Additionally, they can suffer from *oversmoothing* induced by the latent bottleneck, where the reconstructed outputs lack sharpness and fine-details [Takida et al., 2022]. Moreover, we show in this paper that when emulating GPs, the most commonly used spatial priors, the encoder-decoder architecture introduces unnecessary overhead for applications focused solely on inference. Consequently, their adoption in applied fields like disease mapping remains limited, where ease of use, efficiency, and reliability are crucial.

In practice, disease mapping workflows often rely either on fast, black-box tools such as R-INLA [Lindgren and Rue, 2015], or slow, bespoke models using Probabilistic Programming Languages (PPLs) [Carpenter et al., 2017, Abril-Pla et al., 2023, Phan et al., 2019, Bingham et al., 2019, de Valpine et al., 2017]. While PPLs offer flexibility and robust inference via Markov Chain Monte Carlo (MCMC), their performance and computational demands suffer when modeling large spatial datasets, particularly when using Gaussian processes. This trade-off between computational efficiency and model flexibility creates a need for novel

1 INTRODUCTION

Bayesian modeling serves as a fundamental framework analyzing spatial data, particularly in disease mapping, where Gaussian processes (GPs) [Williams and Rasmussen, 2006] and its close relatives, such as the conditional autoregressive (CAR, Besag [1974]), the Intrinsic Conditional Auto-Regressive (ICAR, Besag and Kooperberg [1995]), and Besag-Yorg-Mollie (BYM, Besag et al. [1991]) models are frequently employed to capture spatial dependencies. However, sampling from these models incurs a computational complexity of $\mathcal{O}(n^3)$, as inverting the covariance matrix is required, posing scalability challenges for

solutions that integrate the benefits of pre-trained priors with practical usability for spatial modeling.

To address these challenges, we introduce **DeepRV**, a novel training procedure and architecture that simplifies spatial modeling. Rather than using realizations of the stochastic process as training data for pre-trained priors, our approach utilizes the latent space as training input, enabling DeepRV to directly map the latent variables to the prior space. This eliminates the need for an encoder, reducing oversmoothing, lowering the parameter count, simplifying training, and accelerating inference while preserving prior richness. Our contributions are threefold:

- *The novel **DeepRV** architecture and training process:* A decoder-only generative model that improves performance and accelerates training compared to VAE-based methods. Additionally, we incorporate the gated multi-layer perceptron (gMLP) [Liu et al., 2021], further improving the model’s ability to capture complex spatial dependencies while maintaining efficiency.
- *UK and Zimbabwe case-studies:* We demonstrate the efficacy of DeepRV on both simulated data for UK Lower Tier Local Authorities (LTLA) and real-world datasets, including the 2016 HIV prevalence in Zimbabwe and 2023 cancer mortality rates in UK Local Authority Districts (LAD). Our results highlight significant speedups and robust inference performance compared to full MCMC sampling in NumPyro.
- *API for practical usability:* we provide code for generating pre-trained priors, bridging the gap between methodological advances in Bayesian modeling and their practical application in disease mapping.

Our results show that inference with DeepRV in NumPyro is faster and more scalable than directly sampling GPs, while maintaining comparable performance. By addressing key computational and usability challenges, DeepRV lays the foundation for broader adoption of pre-trained priors in Bayesian inference workflows.

2 VAE-BASED ENCODING PRIORS

PriorVAE [Semenova et al., 2022] and π VAE [Mishra et al., 2022] are two related VAE-based methods, with PriorVAE encoding finite realizations of stochastic processes and π VAE capturing their continuous representations. They use a two-stage approach where a VAE decoder, pre-trained to approximate complex priors, is used for sampling within Bayesian inference with MCMC – preserving MCMC rigor while enhancing scalability. π VAE learns low-dimensional embeddings of function classes inspired by the Karhunen–Loève expansion, where basis functions are learned via a neural network, and random coefficients are encoded with a VAE. PriorVAE, in contrast, follows a standard VAE frame-

work to encode finite realizations of a stochastic prior in question, such as GPs realizations, commonly used in spatial statistics. A key limitation of π - and PriorVAE is their inability to encode and infer hyperparameters of the stochastic process. PriorCVAE [Semenova et al., 2023b] addresses this by introducing a conditional VAE (CVAE) architecture [Sohn et al., 2015], allowing priors to be conditioned on parameters of interest by incorporating them into both encoder and decoder inputs. This enhances prior flexibility and enables parameter inference. The PriorCVAE workflow is presented in the Appendix, Algorithm 2. However, PriorCVAE still suffers from VAE limitations such as posterior collapse and oversmoothing, limiting practical usability. In this work, we build on PriorCVAE to develop a simplified approach for conditioning and sampling pre-trained stochastic process priors.

3 THE PROPOSED METHOD: DEEPRV

In this section, we introduce **DeepRV**, a decoder-only deep generative model that efficiently trains approximate spatial priors for inference, enhancing parameter estimation in MCMC compared to existing methods. Unlike VAEs, which map inputs to a latent space and reconstruct samples via a learned decoder, DeepRV directly maps a fixed latent distribution to realizations of stochastic processes. While this choice restricts the range of processes the network can encode, as it relies on prior knowledge of the mapping between the latent space and realizations. However, its specialization leads to clear performance improvements over VAE-based approaches while still effectively emulating a broad class of spatial priors, including the widely used GPs. The design of PriorCVAE and DeepRV are illustrated in Figure 1, highlighting their shared data generation process (Figure 1, a), and their structural differences (Figure 1, b-c).

3.1 TRAINING AND INFERENCE WORKFLOW

The first step of the DeepRV workflow approximates realizations of the stochastic process $F_{\mathbf{c}}(\cdot)$, conditioned on hyperparameters $\mathbf{c} \sim p_{\mathcal{C}}(\cdot)$, at a fixed set of n locations $\mathbf{x} = (x_1, \dots, x_n)^\top$ within the index set. By $\mathbf{f}_{\mathbf{c}} = F_{\mathbf{c}}(\mathbf{x})$, we denote the vector of realizations of the process at the fixed locations \mathbf{x} , which forms a *random variable* – hence the “RV” abbreviation in the method’s name. To model these realizations, a latent space $\mathcal{Z} \subseteq \mathbb{R}^n$ is introduced, along with a probability distribution $\mathcal{D}_{\mathcal{Z}}(\cdot)$ over this space and a deterministic mapping $T_{\mathbf{c}}$. The map $T_{\mathbf{c}}$ is defined such that when applied on latent samples $\mathbf{z} \sim \mathcal{D}_{\mathcal{Z}}(\cdot)$, it generates outputs distributed according to the stochastic process realizations $\mathbf{f}_{\mathbf{c}}$. We train a deep neural network – hence the “Deep” abbreviation in the method’s name – to approximate $T_{\mathbf{c}}$ by minimizing the reconstruction loss between the true

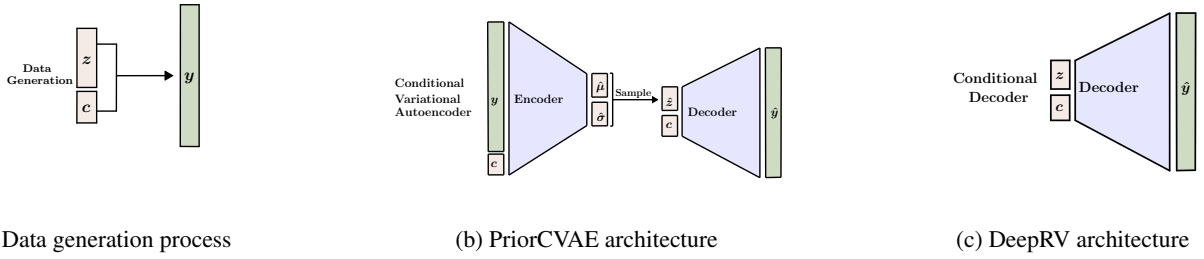


Figure 1: (a) Data generation process; (b) PriorCVAE architecture: both the encoder and decoder get the label c as input. Here we interpret c as a hyperparameter of the prior; (c) deepRV architecture.

process realization \mathbf{f}_c and the model-generated output $\hat{\mathbf{f}}_c$:

$$\begin{aligned} \mathbf{c} &\sim p_c(\cdot), \quad \mathbf{z} \sim \mathcal{D}_z(\cdot), \\ \mathbf{f}_c &= T_c(\mathbf{z}), \quad \hat{\mathbf{f}}_c = \text{DeepRV}(\mathbf{z}, \mathbf{c}), \\ \mathcal{L}_{\text{DeepRV}} &= \text{MSE}(\mathbf{f}_c, \hat{\mathbf{f}}_c). \end{aligned} \quad (1)$$

After training, the inference process involves replacing the realizations of the stochastic process F_c , \mathbf{f}_c , by sampling from the latent distribution $\mathcal{D}_z(\cdot)$, the hyperparameter priors $p_c(\cdot)$, and feeding them into the trained DeepRV network to generate posterior samples:

$$\mathbf{c} \sim p_c(\cdot), \quad \mathbf{z} \sim \mathcal{D}_z(\cdot), \quad \mathbf{f}_c \approx \hat{\mathbf{f}}_c = \text{DeepRV}(\mathbf{z}, \mathbf{c}).$$

DeepRV is not restricted to any specific architecture—any network that accepts a latent variable and conditional variables, and outputs a matching stochastic process can serve as the decoder.

3.2 SUPPORTED PRIORS

The training procedure relies on prior knowledge of a mapping function T_c that directly links the latent space to process realizations. While this design imposes more constraints than standard VAEs, it still enables DeepRV to encode complex priors. The most natural application of DeepRV is GPs, a broad class of highly expressive and popular stochastic processes. To adapt a GP with a kernel \mathbf{K}_c to DeepRV’s training framework, we set the latent space $\mathcal{Z} = \mathbb{R}^n$, $\mathcal{D}_z = \mathcal{N}(\mathbf{0}, \mathbf{I})$, and define $T_c(\mathbf{z}) = \mathbf{L}_c \mathbf{z}$, where $\mathbf{L}_c = \text{Cholesky}(\mathbf{K}_c)$. The distribution of $\mathbf{L}_c \mathbf{z}$ when sampling $\mathbf{z} \sim \mathcal{N}(\mathbf{0}, \mathbf{I})$ is equivalent to $\mathcal{MVN}(\mathbf{0}, \mathbf{K}_c)$, ensuring the correct mapping from the latent space to the GP realizations. A complete, generalized GP workflow example is provided in Algorithm 1.

Beyond GPs, DeepRV can also be applied to other spatial models, such as CAR, ICAR, and BYM, as they can similarly be represented as mappings of a latent variable \mathbf{z} and parameters \mathbf{c} . Eventually, we plan to expand this to any process that can be represented functionally as: $(\mathbf{z}, \mathbf{c}) \rightarrow \mathbf{f}_c$.

This would enable modeling not just GPs, but whole hierarchical models or even black box simulators, although this is beyond the scope of the current study and left for future research. An example DeepRV workflow with a hierarchical model is provided in Appendix B.

4 EXPERIMENTS

This section presents the experiments conducted on simulated and real datasets. These involve training DeepRV across multiple spatial priors, evaluating the resulting models using Empirical Bayes, and performing inference. DeepRV’s codebase is available in the following repository¹. The API is designed to accept a GeoPandas [Jordahl et al., 2023]-compatible map, and the maps used in these experiments can be accessed via the map download link².

4.1 ARCHITECTURE

In this paper, we employ two decoder architectures to implement DeepRV. First, we use a simple two-layer MLP without dimensionality reduction to maintain consistency with previous models, enabling straightforward comparison. This choice emphasizes that our primary contribution lies in the novel training process and the decoder-only architecture, rather than architectural complexity. However, MLPs struggle to learn the identity function, which poses challenges when reconstructing realizations, particularly when spatial correlation is low (*e.g.*, small lengthscales in GPs). To address this, we employ a gated multi-layer (gMLP) perceptron [Liu et al., 2021] architecture, which, by leveraging gating mechanisms and residual connections, improves reconstruction capabilities in these scenarios.

¹<https://drive.google.com/file/d/1LAVM9E8p34DKe2BCmtIR0b8PPyTVg2gD/view?usp=sharing>

²<https://drive.google.com/file/d/15DAfsL5dtO-lM3ef0saJ-73hMcQx6XVK/view?usp=sharing>

Algorithm 1 DeepRV GP workflow example

Fix the **spatial structure** of interest $\mathbf{x} = (x_1, \dots, x_n)$, *e.g.* centroids of administrative units
Fix the **GP** of interest, *i.e.* a kernel $k_{\mathbf{c}}(\cdot, \cdot)$

Train DeepRV prior:

- Sample hyperparameters: $\mathbf{c} \sim p_{\mathbf{c}}(\cdot)$
- Sample GP realizations:
 - Generate $\mathbf{K}_{\mathbf{c}} = k_{\mathbf{c}}(\mathbf{x}, \mathbf{x})$ over the spatial structure \mathbf{x}
 - Compute the Cholesky factor $\mathbf{L}_{\mathbf{c}} = \text{Cholesky}(\mathbf{K}_{\mathbf{c}})$
 - Sample $\mathbf{z} \sim \mathcal{N}(\mathbf{0}, \mathbf{I})$, and set $\mathbf{f}_{\mathbf{c}} = \mathbf{L}_{\mathbf{c}}\mathbf{z}$
- Forward pass: $\hat{\mathbf{f}}_{\mathbf{c}} = \text{DeepRV}(\mathbf{z}, \mathbf{c})$
- Back propagate the loss: $\mathcal{L}_{\text{DeepRV}} = \text{MSE}(\mathbf{f}_{\mathbf{c}}, \hat{\mathbf{f}}_{\mathbf{c}})$

Perform Bayesian inference with MCMC of the overarching model, including latent variables and hyperparameters \mathbf{c} in a drop-in manner using the trained network:

$$\mathbf{f}_{\mathbf{c}} \sim \mathcal{GP}_{\mathbf{c}}(\cdot, \cdot) \approx \hat{\mathbf{f}}_{\mathbf{c}} = \text{DeepRV}(\mathbf{z}, \mathbf{c}), \mathbf{z} \sim \mathcal{N}(\mathbf{0}, \mathbf{I})$$

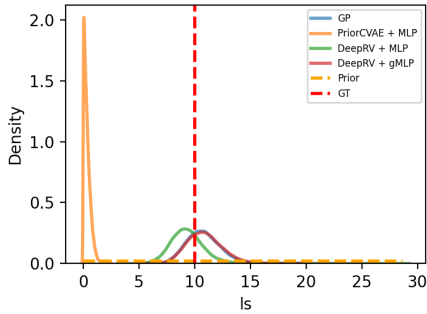


Figure 2: Simulated data inference - posterior predictive of lengthscale distribution for the Matérn 1/2 Kernel

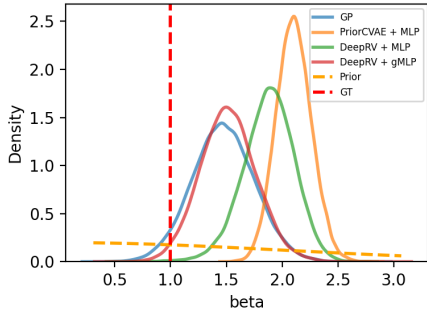


Figure 3: Simulated data inference - posterior predictive of the fixed effects (β) distribution for the Matérn 1/2 Kernel

4.2 SIMULATION STUDY: UK LTLAS

4.2.1 Data

The geographical structure consists of 363 Lower Tier Local Authorities (LTLAs) from the UK, with data simulated using the centroids of each LTLA. We simulate data over this map because the number of locations ($n = 363$) is al-

ready challenging for GPs but still manageable to enable benchmarking against MCMC with GP sampling, while still representing a standard structure used in disease mapping. This enables us to assess the real-world applicability of our method and quantify the inference speedups it achieves. The coordinates of the centroids are normalized to a $[0,100]$ range and serve as spatial structure for DeepRV’s GP workflow (see Algorithm 1). We also experimented with the CAR prior, which relies on an underlying graph structure of the data. An adjacency matrix is constructed by connecting neighboring LTLAs, ensuring that islands are linked to the nearest LTLA to maintain a fully connected graph.

4.2.2 Prior Pre-training

We trained the DeepRV and PriorCVAE models to emulate GP priors across four distinct kernels: RBF, Matérn-3/2, Matérn-1/2, Matérn-5/2, and the CAR model. For the RBF and Matérn kernels, we defined hyperparameter priors with constant variance and lengthscales drawn from $\text{Uniform}(0.0, 50.0)$ for RBF, and the Matérn kernels. The lengthscale ranges for the RBF and Matérn kernels were chosen to produce very sharp (lengthscale ≈ 0), to very smooth (lengthscale ≈ 50) spatial correlations. For the CAR model, we set $\tau = 1$ and α is sampled from $\text{Beta}(4, 1)$, where

$$\mathbf{f}_{\text{CAR},\tau,\alpha} \sim \mathcal{MVN}(\mathbf{0}, \mathbf{R}^-), \quad \mathbf{R} = \tau(\mathbf{D} - \alpha\mathbf{A}).$$

Here, \mathbf{D} represents the degree matrix of the adjacency matrix \mathbf{A} . We compared PriorCVAE and DeepRV by computing the MSE between the process realization \mathbf{f} , and the reconstructed realization $\hat{\mathbf{f}}$. We trained the models over 5 random seeds with a batch size of 32, over 100,000 batches. Results of reconstruction MSE, and pre-training running times are summarized in Tables 1 and 2, correspondingly. Additionally, we provide figures in Appendix C to further assess the reconstruction capabilities of these models. These tables

and figures demonstrate that the MLP-based DeepRV model outperforms PriorCVAE in reconstruction quality, despite having 66% fewer parameters while using the same MLP architecture. Notably, PriorCVAE has access to the full process realization as input, whereas DeepRV operates solely on latent variables, highlighting its efficiency in learning structured priors. Furthermore, the gMLP-based DeepRV further improves reconstruction across all processes except RBF, with particularly strong performance on sharper kernels and lower length scales (see Table 3).

Table 1: Prior pre-training test MSE($\mathbf{f}, \hat{\mathbf{f}}$)

Spatial Prior Parameters	PriorCVAE	DRV + gMLP	DRV + MLP
	794,244	298,441	264,990
CAR	0.381 ± 0.005	0.014 ± 0.003	0.033 ± 0.004
Matérn-5/2	0.164 ± 0.002	0.019 ± 0.005	0.040 ± 0.001
Matérn-1/2	0.295 ± 0.003	0.004 ± 0.001	0.046 ± 0.001
Matérn-3/2	0.182 ± 0.003	0.012 ± 0.004	0.039 ± 0.001
RBF	0.102 ± 0.001	0.047 ± 0.003	0.034 ± 0.001

Table 2: Prior pre-training runtime (seconds)

Spatial Prior Parameters	PriorCVAE	DRV + gMLP	DRV + MLP
	794,244	298,441	264,990
CAR	532.8 ± 15.1	591.8 ± 1.9	506.0 ± 2.3
Matérn-5/2	363.2 ± 1.9	410.4 ± 1.1	332.4 ± 0.9
Matérn-1/2	362.6 ± 1.7	408.6 ± 1.8	333.8 ± 2.7
Matérn-3/2	362.6 ± 0.9	410.0 ± 1.6	335.6 ± 2.7
RBF	366.8 ± 4.9	414.6 ± 1.8	340.8 ± 1.3

To evaluate the pre-trained priors we employ an Empirical Bayes (EB) approach. Specifically, we generate samples from either the surrogate model or a reference GP model using predefined hyperparameters, adding independent noise $\boldsymbol{\sigma} \sim \mathcal{N}(\mathbf{0}, \sigma \mathbf{I})$ to achieve a Gaussian Likelihood. These samples serve as pseudo-observations, and we subsequently optimize the hyperparameters to maximize the marginal likelihood [Williams and Rasmussen, 2006]. The full procedure for sampling from DeepRV and estimating GP hyperparameters with kernel \mathbf{K} is as follows:

$$\begin{aligned}
 \mathbf{c} &\sim p_{\mathbf{c}}(\cdot), \mathbf{z} \sim \mathcal{N}(\mathbf{0}, \mathbf{I}), \boldsymbol{\sigma} \sim \mathcal{N}(\mathbf{0}, \sigma \mathbf{I}), \\
 \mathbf{f}_{\mathbf{c}} &\sim \text{DeepRV}(\mathbf{c}, \mathbf{z}) + \boldsymbol{\sigma}, \\
 \mathbf{y} &= -\frac{1}{2} \mathbf{f}_{\mathbf{c}}^{\top} \tilde{\mathbf{K}}_{\hat{\mathbf{c}}}^{-1} \mathbf{f}_{\mathbf{c}} - \frac{1}{2} \log |\tilde{\mathbf{K}}_{\hat{\mathbf{c}}}| - \frac{n}{2} \log 2\pi, \\
 \hat{\mathbf{c}}, \hat{\sigma} &= \text{argmax}_{\mathbf{c}, \sigma} (\mathbf{y}), \\
 \tilde{\mathbf{K}}_{\hat{\mathbf{c}}} &= \mathbf{K}_{\hat{\mathbf{c}}} + \text{Diag}(\hat{\sigma}).
 \end{aligned}$$

This process allows us to assess how closely the priors, learned via the surrogate models, emulate the behavior of true GP priors. We generated 100 samples for each of 5 random seeds and computed the mean squared error (MSE) between the true conditional variable (lengthscale or α) and the estimated value obtained via EB. The results are presented in the Appendix, Section C.2. This process also

Table 3: Small lengthscale [0, 5]: MSE($\mathbf{f}, \hat{\mathbf{f}}$)

Kernel	PriorCVAE	DRV + gMLP	DRV + MLP
Matérn-5/2	0.778 ± 0.01	0.074 ± 0.01	0.252 ± 0.01
Matérn-1/2	0.821 ± 0.00	0.017 ± 0.00	0.240 ± 0.01
Matérn-3/2	0.785 ± 0.01	0.049 ± 0.01	0.232 ± 0.01
RBF	0.374 ± 0.011	0.15 ± 0.010	0.187 ± 0.00

underscores the simplicity of inference under a Gaussian likelihood. Therefore, we extend our analysis to more complex likelihoods for both simulated and real-world data.

4.2.3 Inference

After training the priors, we assessed their ability to emulate a GP within a Numpyro model for inference. We simulated data across UK’s LTLAs using the following Poisson model, which was also employed as our inference model:

$$\begin{aligned}
 \mathbf{c} &\sim p_{\mathbf{c}}(\cdot), \\
 \mathbf{f}_{\mathbf{c}} &\sim \mathcal{GP}_{\mathbf{c}}(\cdot), \\
 \beta &\sim \mathcal{N}(0, 1), \\
 \boldsymbol{\lambda} &= \exp(\beta + \mathbf{f}_{\mathbf{c}}) \\
 \mathbf{y}_{\mathbf{c}} &\sim \text{Poisson}(\boldsymbol{\lambda}).
 \end{aligned} \tag{2}$$

During inference, the pre-trained prior $\hat{\mathbf{f}}_{\mathbf{c}}$ was used as a substitute for Eq. 2, replacing the computationally intensive GP sampling during MCMC. We employed the No-U-Turn Sampler (NUTS) [Hoffman and Gelman, 2014] algorithm for MCMC implemented in Numpyro, running 4 chains with 4,000 warmup iterations and collecting 10,000 posterior samples per chain. We specified the prior distributions to ensure appropriate regularization and flexibility in modeling spatial dependencies. For all distance-based GP kernels, we placed a uniform prior on the lengthscale, $\text{Uniform}(0, 50)$, allowing a wide range of spatial correlations. For the CAR prior, we set $\alpha \sim \text{Beta}(4, 1)$ to encourage strong but not deterministic spatial dependence. The prior for the fixed effects, β , was set as $\mathcal{N}(\mathbf{0}, 2\mathbf{I})$, providing a weakly informative Gaussian prior.

To generate the simulated observed data, we set $\beta = 1$ and lengthscale = 10, where the low lengthscale results in sharp, challenging samples, while $\beta = 1$ ensures a relatively broad range of counts across the LTLAs, making the simulation more realistic. For the CAR model, we chose $\alpha = 0.95$ to maintain strong spatial correlation between LTLAs. The results are presented in Table 4, Figure 2, and in the Appendix Section D. The results show that DeepRV consistently matches the performance of full GP sampling within MCMC while achieving lower MSE than PriorCVAE, indicating closer mean estimates. Additionally, inference remains 2× faster than full GP sampling, with this advantage expected to grow as the number of locations increases.

Table 4: Simulated data inference results. The mean inferred parameters closest to the true values, the lowest mean sample-to-real sample MSE, the shortest inference times are **bolded**, and the mean ESS of the spatial correlation samples f_c .

		CAR (α - Eq 4.2.2)	Matérn-1/2 (lengthscale)	Matérn-3/2 (lengthscale)	Matérn-5/2 (lengthscale)	RBF (lengthscale)
	True Parameter Value	0.95	10	10	10	10
GP	Inferred Parameter Mean	0.940	10.770	10.057	9.628	9.954
	MSE (y, \bar{y}_{pred})	1.918	3.044	6.985	8.930	13.226
	ESS Inferred Variable	15,331	17,304	18,289	16,927	20,621
	Mean ESS f_c	59,804	27,784	22,481	20,077	18,634
	Runtime (s)	1,716	3,804	4,044	3,998	4,157
	Mean ESS f_c per second	34.85	7.3	5.56	5.02	4.48
PriorCVAE	Inferred Parameter Mean	0.793	0.346	0.716	0.610	2.243
	MSE (y, \bar{y}_{pred})	18.593	538.303	380.696	321.735	250.331
	ESS Inferred Variable	55,204	36,933	26,719	15,788	11,079
	Mean ESS f_c	47,288	24,119	24,244	15,369	20,352
	Runtime (s)	793	984	969	987	979
	Mean ESS f_c per second	59.63	24.51	25.02	15.57	20.79
DRV + MLP	Inferred Parameter Mean	0.816	9.437	9.489	8.082	8.526
	MSE (y, \bar{y}_{pred})	3,586.445	69.788	17.465	19.236	21.542
	ESS Inferred Variable	46,094	3,997	6,988	9,543	8,133
	Mean ESS f_c	40,353	17,175	21,847	20,212	9,651
	Runtime (s)	272	856	1,091	1,096	781
	Mean ESS f_c per second	148.36	20.06	20.02	18.44	12.36
DRV + gMLP	Inferred Parameter Mean	0.942	10.875	10.378	10.151	9.712
	MSE (y, \bar{y}_{pred})	2.071	5.577	10.354	17.636	35.266
	ESS Inferred Variable	13,465	13,724	14,978	17,732	12,730
	Mean ESS f_c	60,080	23,277	20,146	21,195	19,275
	Runtime (s)	540	1,347	1,533	2,352	1,523
	Mean ESS f_c per second	111.26	17.28	13.14	9.01	12.66

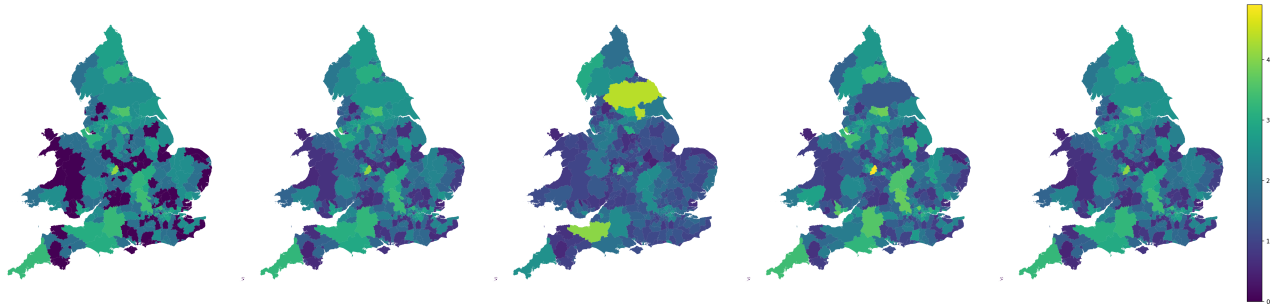


Figure 4: Female under 50 cancer mortality log-scaled count y vs. mean posterior predictive sample \hat{y} for the Matérn 1/2 kernel. (a) Observed counts, (b) GP (c) PriorCVAE, (d) DeepRV + MLP, (e) DeepRV + gMLP.

4.3 REAL-LIFE DATA

4.3.1 Data

We utilized cancer mortality data for females and males under the age of 50 across 318 Local Authority Districts (LADs) in England and Wales. The data was extracted from the UK Office for National Statistics (ONS) Nomis

database³. The records were queried based on the 2021 LAD boundaries by age and gender, then mapped to 2023 LADs using a translation map available on the ONS Geoportal⁴. This was necessary due to incomplete census population data for the 2021 LADs, which prevented the application

³<https://www.nomisweb.co.uk/query/construct/summary.asp?mode=construct&version=0&dataset=161>

⁴https://geoportal.statistics.gov.uk/datasets/32e1e25b27d7472da86a250c5f0c2d2d_0

Table 5: Real data inference results. The mean inferred lengthscale, variance and fixed effect closest to the full GP mean, the lowest mean sample-to-real sample MSE, the shortest inference times are **bolded**, and the mean ESS of the GP samples.

	Dataset GP Kernel	Female U50 cancer mortality		Male U50 cancer mortality		Zimb-HIV
		Matérn-1/2	Matérn-3/2	Matérn-1/2	Matérn-3/2	Matérn-1/2
GP	Inferred Lengthscale Mean	0.615	0.582	0.578	0.395	72.388
	Inferred Fixed Effects Mean	-4.666	-4.667	-5.251	-5.252	-1.673
	Inferred Variance Mean	0.696	0.694	1.069	1.059	0.330
	MSE($\mathbf{y}, \bar{\mathbf{y}}_{\text{pred}}$)	1.069	1.070	0.678	0.674	11.699
	ESS Lengthscale	1,788	4,727	2,785	434	24,823
	Mean ESS GP f_c	29,172	44,052	40,220	4,382	14,969
	Runtime (s)	1,217	1,288	1,467	1,270	1,460
	Mean ESS f_c per second	23.97	34.20	27.42	3.45	10.25
PriorCVAE	Inferred Lengthscale Mean	0.291	0.344	0.243	0.283	0.487
	Inferred Fixed Effects Mean	-4.981	-4.559	-4.370	-4.277	-1.615
	Inferred Variance Mean	0.123	0.208	0.122	0.223	0.900
	MSE($\mathbf{y}, \bar{\mathbf{y}}_{\text{pred}}$)	59.458	127.083	129.437	204.164	1620.774
	ESS Lengthscale	42,217	45,473	49,598	45,282	3,778
	Mean ESS GP f_c	12,008	11,668	19,803	15,147	19,160
	Runtime (s)	1,333	1,524	903	935	754
	Mean ESS f_c per second	9.00	7.66	21.93	16.20	25.41
DeepRV + MLP	Inferred Lengthscale Mean	1.299	0.662	3.691	2.524	57.497
	Inferred Fixed Effects Mean	-4.451	-4.453	-4.892	-4.933	-1.773
	Inferred Variance Mean	1.077	0.889	1.702	2.022	0.614
	MSE($\mathbf{y}, \bar{\mathbf{y}}_{\text{pred}}$)	70.362	69.673	53.328	69.740	11.954
	ESS Lengthscale Mean	10,726	13,038	11,086	7,277	2,440
	Mean ESS GP f_c	24,047	13,382	22,306	30,410	9,912
	Runtime (s)	941	900	1,003	1,188	1,438
	Mean ESS f_c per second	25.55	14.87	22.24	25.60	6.89
DeepRV + gMLP	Inferred Lengthscale Mean	0.763	0.458	0.543	0.388	74.012
	Inferred Fixed Effects Mean	-4.683	-4.669	-5.251	-5.234	-1.707
	Inferred Variance Mean	0.688	0.652	1.047	0.990	0.330
	MSE($\mathbf{y}, \bar{\mathbf{y}}_{\text{pred}}$)	1.487	1.514	0.882	0.942	12.676
	ESS Lengthscale	7,180	362	7,106	4,399	22,170
	Mean ESS GP f_c	71,553	10,821	63,809	47,206	12,998
	Runtime (s)	845	898	842	860	1,679
	Mean ESS f_c per second	84.68	12.05	75.78	54.89	7.74

of population-dependent models such as Binomial models. We conducted inference independently for each gender. We also examined HIV prevalence data from the 2015–2016 Population-Based HIV Impact Assessment Survey in Zimbabwe [Sachathep et al., 2021], comprising 63 locations. DeepRV was pretrained, followed by inference and benchmarking against a full GP sample. For all datasets we set our spatial structure as the normalized [0-100] centroids of the location data, by the procedure outlined in Section 4.2.1.

4.3.2 Inference

We followed the pre-training and inference procedures described in Section 4.2, using the Matérn-1/2, and Matérn-3/2 kernels to train the DeepRV models for emulating GP samples over the centroids. For the UK case-study, we specified a flexible pre-training prior for the

length scale as Uniform(0, 50) and for the variance using a Gamma(1.5, 1.5) prior. For the Zimbabwe HIV prevalence dataset, we extended the lengthscale range to Uniform(0, 100) due to inference results indicating the need for a broader prior distribution. We performed inference using a Binomial model, incorporating fixed effects while capturing spatial correlations through a GP. This choice is motivated by the nature of the data, which consists of count data with varying population sizes across locations, represented by \mathbf{N} . Lastly, in the cancer mortality datasets, we scaled down \mathbf{N} by a factor of 100 to improve numerical stability, as the large population sizes relative to mortality counts led to extremely low prevalence values (\mathbf{p}). The model is specified as follows:

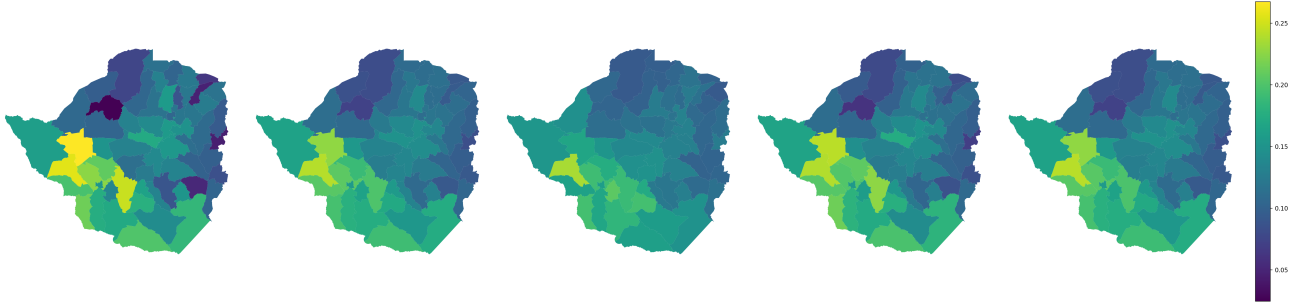


Figure 5: Zimbabwe HIV prevalence \mathbf{p} vs. estimated $\hat{\mathbf{p}}$ for the Matérn-1/2 kernel. (a) Observed counts, (b) GP (c) PriorCVAE, (d) DeepRV + MLP, (e) DeepRV + gMLP.

$$\begin{aligned}
 \text{var, ls} : \mathbf{c} &\sim p_{\mathbf{c}}(\cdot), \\
 \mathbf{z} &\sim \mathcal{MVN}(\mathbf{0}, \mathbf{I}) \\
 \mathbf{f}_{\mathbf{c}} &= \text{DeepRV}(\mathbf{z}, \mathbf{c}) \\
 \beta &\sim \mathcal{N}(0, 1) \\
 \mathbf{p} &= \text{logit}^{-1}(\beta + \mathbf{f}_{\mathbf{c}}) \\
 \mathbf{y}_{\text{Binom}, \mathbf{c}} &\sim \text{Binom}(\mathbf{N}, \mathbf{p})
 \end{aligned} \tag{3}$$

The results are presented in Table 5 and Figures 4, 5, where we further benchmark DeepRV against PriorCVAE and full GP sampling. Additional figures can be found in Appendix E. These results demonstrate how closely DeepRV, particularly the gMLP variant, matches full GP sampling, both for very low lengthscales (cancer mortality) and high lengthscales (Zimbabwe HIV prevalence). Additionally, DeepRV achieves a 1.5 \times faster runtime across all inference runs, except for Zimbabwe HIV, where the smaller sample size ($n = 63$) limits speedup gains.

5 DISCUSSION AND FUTURE WORK

The pre-training results summarized in Tables 1, 2, demonstrate that DeepRV surpasses PriorCVAE in reconstructing GP realizations. Table 9 further confirms that DeepRV’s pre-trained prior more closely aligns with the emulated GP, a pattern that continues through inference (Table 4). We attribute this improvement to two main factors. First, DeepRV’s training objective prioritizes input reconstruction over balancing reconstruction with encoder KL loss minimization. This focus is reinforced by the performance gains observed in both DeepRV and its MLP variant over PriorCVAE, which shares the same MLP-based encoder-decoder architecture. Second, the gMLP Liu et al. [2021] variant of DeepRV further enhances performance by effectively handling smaller lengthscales, as discussed in Section 4.1. This advantage is further supported by results in Table 3 and additional findings in the Appendix (Tables 6, 7, 8).

Furthermore, inference on both simulated and real-world datasets (Tables 4, 5 and Figures 2, 4, 5) demonstrates

that DeepRV produces posterior estimates closely matching those obtained via GP sampling. In some cases, DeepRV even recovers values closer to the true data-generating process while achieving up to a 2 \times speedup. This performance holds consistently across all tested spatial priors, as further evidenced in Appendix D.

In the short term, we intend to characterize more precisely which priors DeepRV can encode to fully capture the potential of this framework. Further, we will explore DeepRV’s ability to model full hierarchical structures, as demonstrated in Appendix 3, and evaluate its scalability to finer administrative divisions, such as UK Middle Layer Super Output Areas (MSOA) [Rashid et al., 2021]. Long term, we plan to expand our library of pretrained priors to cover various administrative levels within the UK (e.g., LTLA, LAD, MSOA, postcode-level) and extend support to other regions.

This study faces some limitations. DeepRV improves efficiency but still relies on costly sampling methods to generate training data, particularly the cubic complexity of GP kernel computations, which can lead to out-of-memory (OOM) issues and hinder scalability when training with many locations. Like VAEs, it requires a predefined spatial structure, which can be restrictive in certain applications. However, unlike VAEs, DeepRV cannot encode arbitrary processes; instead, it relies on prior knowledge of a mapping function that directly links the latent space to process realizations. Attempts to benchmark against Laplace approximation and ADVI proved challenging due to their sensitivity to tuning, leading to unreliable inferences. Future work should explore these alternatives and simulation-based inference for improved evaluation, as well as metrics beyond MSE to better assess the performance of pretrained priors during training.

DeepRV represents a step toward more efficient and scalable probabilistic modeling by leveraging pre-trained priors without the need for full GP sampling. Its ability to accelerate inference while closely approximating the GPs rigor, and integrate seamlessly with PPLs highlights its potential for broader adoption. Future research will focus on refining its applicability across domains, improving its scalability, and benchmarking it against alternative inference strategies.

Acknowledgments

J.N. and E.S. acknowledge support in part by the AI2050 program at Schmidt Sciences (Grant [G-22-64476]). J.N. and S.F. acknowledge the EPSRC (EP/V002910/1). D.J. acknowledges his Google DeepMind scholarship. We thank Tom Rainforth for advice on the method and James Bennett for advice on data access. We thank Paolo Andrich for his feedback on the manuscript.

References

- Oriol Abril-Pla, Virgile Andreani, Colin Carroll, Larry Dong, Christopher J Fonnesebeck, Maxim Kochurov, Ravin Kumar, Junpeng Lao, Christian C Luhmann, Osvaldo A Martin, et al. Pymc: a modern, and comprehensive probabilistic programming framework in python. *PeerJ Computer Science*, 9:e1516, 2023.
- Julian Besag. Spatial interaction and the statistical analysis of lattice systems. *Journal of the Royal Statistical Society: Series B (Methodological)*, 36(2):192–225, 1974.
- Julian Besag and Charles Kooperberg. On conditional and intrinsic autoregressions. *Biometrika*, 82(4):733–746, 1995.
- Julian Besag, Jeremy York, and Annie Mollié. Bayesian image restoration, with two applications in spatial statistics. *Annals of the institute of statistical mathematics*, 43:1–20, 1991.
- Eli Bingham, Jonathan P. Chen, Martin Jankowiak, Fritz Obermeyer, Neeraj Pradhan, Theofanis Karaletsos, Rohit Singh, Paul A. Szerlip, Paul Horsfall, and Noah D. Goodman. Pyro: Deep universal probabilistic programming. *J. Mach. Learn. Res.*, 20:28:1–28:6, 2019. URL <http://jmlr.org/papers/v20/18-403.html>.
- Bob Carpenter, Andrew Gelman, Matthew D Hoffman, Daniel Lee, Ben Goodrich, Michael Betancourt, Marcus A Brubaker, Jiqiang Guo, Peter Li, and Allen Riddell. Stan: A probabilistic programming language. *Journal of statistical software*, 76, 2017.
- Perry de Valpine, Daniel Turek, Christopher Paciorek, Cliff Anderson-Bergman, Duncan Temple Lang, and Ras Bodik. Programming with models: writing statistical algorithms for general model structures with NIMBLE. *Journal of Computational and Graphical Statistics*, 26: 403–413, 2017. doi: 10.1080/10618600.2016.1172487.
- Matthew D Hoffman and Andrew Gelman. The no-u-turn sampler: Adaptively setting path lengths in hamiltonian monte carlo. *Journal of Machine Learning Research*, 15 (1):1593–1623, 2014.
- K. Jordahl, J. Van den Bossche, M. Fleischmann, B. McBride, J. Wasserman, T. Toledo, M. Perry, C. Farmer, G.A. Hjelle, and J. Gerard. Geopandas: Python tools for geographic data. <https://geopandas.org>, 2023.
- Diederik P Kingma. Auto-encoding variational bayes. *arXiv preprint arXiv:1312.6114*, 2013.
- Finn Lindgren and Håvard Rue. Bayesian spatial modelling with r-inla. *Journal of statistical software*, 63(19), 2015.
- Hanxiao Liu, Zihang Dai, David So, and Quoc V Le. Pay attention to mlps. *Advances in neural information processing systems*, 34:9204–9215, 2021.
- James Lucas, George Tucker, Roger B Grosse, and Mohammad Norouzi. Don't blame the elbo! a linear vae perspective on posterior collapse. In H. Wallach, H. Larochelle, A. Beygelzimer, F. d'Alché-Buc, E. Fox, and R. Garnett, editors, *Advances in Neural Information Processing Systems*, volume 32. Curran Associates, Inc., 2019. URL https://proceedings.neurips.cc/paper_files/paper/2019/file/7e3315fe390974fcf25e44a9445bd821-Paper.pdf.
- Swapnil Mishra, Seth Flaxman, Tresnia Berah, Mikko Pakkanen, Harrison Zhu, and Samir Bhatt. *pi* vae: Encoding stochastic process priors with variational autoencoders. *Statistics & Computing*, 2022.
- Du Phan, Neeraj Pradhan, and Martin Jankowiak. Composable effects for flexible and accelerated probabilistic programming in numpyro. *arXiv preprint arXiv:1912.11554*, 2019.
- Theo Rashid, James E Bennett, Christopher J Paciorek, Yvonne Doyle, Jonathan Pearson-Stuttard, Seth Flaxman, Daniela Fecht, Mireille B Toledano, Guangquan Li, Hima I Daby, et al. Life expectancy and risk of death in 6791 communities in england from 2002 to 2019: high-resolution spatiotemporal analysis of civil registration data. *The Lancet Public Health*, 6(11):e805–e816, 2021.
- Karampreet Sachathep, Elizabeth Radin, Wolfgang Hladik, Avi Hakim, Suzue Saito, Janet Burnett, Kristin Brown, Neena Phillip, Sasi Jonnalagadda, Andrea Low, Dan Williams, Hetal Patel, Amy Herman-Roloff, Godfrey Musuka, Beth Barr, Nellie Wadondo-Kabonda, Gertrude Chipungu, Yen Duong, Stephen Delgado, Stanley Kamocha, Steve Kinchen, Graham Kalton, Leah Schwartz, George Bello, Owen Mugurungi, Lloyd Mullen, Bharat Parekh, Laura Porter, David Hoos, Andrew Charles Voetsch, and Jessica Justman. Population-based hiv impact assessments survey methods, response, and quality in zimbabwe, malawi, and zambia. *Journal of Acquired Immune Deficiency Syndromes*, 87

(Suppl 1):S6–S16, August 2021. doi: 10.1097/QAI.0000000000002710.

Elizaveta Semenova, Yidan Xu, Adam Howes, Theo Rashid, Samir Bhatt, Swapnil Mishra, and Seth Flaxman. Priorvae: encoding spatial priors with variational autoencoders for small-area estimation. *Journal of the Royal Society Interface*, 19(191):20220094, 2022.

Elizaveta Semenova, Swapnil Mishra, Samir Bhatt, Seth Flaxman, and H Juliette T Unwin. Deep learning and mcmc with aggvae for shifting administrative boundaries: mapping malaria prevalence in kenya. In *International Workshop on Epistemic Uncertainty in Artificial Intelligence*, pages 13–27. Springer, 2023a.

Elizaveta Semenova, Prakhar Verma, Max Cairney-Leeming, Arno Solin, Samir Bhatt, and Seth Flaxman. Priorcvae: scalable mcmc parameter inference with bayesian deep generative modelling. *arXiv preprint arXiv:2304.04307*, 2023b.

Kihyuk Sohn, Honglak Lee, and Xinchen Yan. Learning structured output representation using deep conditional generative models. In C. Cortes, N. Lawrence, D. Lee, M. Sugiyama, and R. Garnett, editors, *Advances in Neural Information Processing Systems*, volume 28. Curran Associates, Inc., 2015. URL https://proceedings.neurips.cc/paper_files/paper/2015/file/8d55a249e6baa5c06772297520da2051-Paper.pdf.

Yuhta Takida, Wei-Hsiang Liao, Chieh-Hsin Lai, Toshimitsu Uesaka, Shusuke Takahashi, and Yuki Mitsufuji. Preventing oversmoothing in vae via generalized variance parameterization. *Neurocomputing*, 509:137–156, 2022. ISSN 0925-2312. doi: <https://doi.org/10.1016/j.neucom.2022.08.067>. URL <https://www.sciencedirect.com/science/article/pii/S0925231222010591>.

Yixin Wang, David Blei, and John P Cunningham. Posterior collapse and latent variable non-identifiability. In M. Ranzato, A. Beygelzimer, Y. Dauphin, P.S. Liang, and J. Wortman Vaughan, editors, *Advances in Neural Information Processing Systems*, volume 34, pages 5443–5455. Curran Associates, Inc., 2021. URL https://proceedings.neurips.cc/paper_files/paper/2021/file/2b6921f2c64dee16ba21ebf17f3c2c92-Paper.pdf.

Christopher KI Williams and Carl Edward Rasmussen. *Gaussian processes for machine learning*, volume 2. MIT press Cambridge, MA, 2006.

A PRIORCVAE WORKFLOW

Algorithm 2 PriorCVAE [Semenova et al., 2023b] workflow

Fix the **spatial structure** of interest $\mathbf{x} = (x_1, \dots, x_n)$, *e.g.* centroids of administrative units

Fix the **latent dimension size** $d \leq n$ for the decoder $D_\psi : \mathbb{R}^d \times \mathcal{C} \rightarrow \mathbb{R}^n$, and the encoder $E_\gamma : \mathbb{R}^n \times \mathcal{C} \rightarrow \mathbb{R}^d$.

Train PriorCVAE prior:

- Sample hyperparameters: $\mathbf{c} \sim p_{\mathcal{C}}(\cdot)$.
- Sample GP realizations: $\mathbf{f}_{\mathbf{c}} \sim \mathcal{GP}_{\mathbf{c}}(\cdot)$, over the spatial structure \mathbf{x}
- Encode $\hat{\mathbf{z}}_\mu, \hat{\mathbf{z}}_\sigma = E_\gamma(\mathbf{f}_{\mathbf{c}}, \mathbf{c})$, sample $\hat{\mathbf{z}} \sim \mathcal{N}(\hat{\mathbf{z}}_\mu, \hat{\mathbf{z}}_\sigma)$, and decode $\hat{\mathbf{f}}_{\mathbf{c}} = D_\psi(\hat{\mathbf{z}}, \mathbf{c})$.
- Back propagate the loss: $\mathcal{L}_{\text{CVAE}} = \frac{1}{\sigma_{\text{vae}}^2} \text{MSE}(\mathbf{f}_{\mathbf{c}}, \hat{\mathbf{f}}_{\mathbf{c}}) + \text{KL}[\mathcal{N}(\hat{\mathbf{z}}_\mu, \hat{\mathbf{z}}_\sigma) || \mathcal{N}(\mathbf{0}, \mathbf{1})]$

Perform Bayesian inference with MCMC of the overarching model, including latent variables and hyperparameters \mathbf{c} , by approximating $f_{\mathbf{c}}$ with $\hat{\mathbf{f}}_{\mathbf{c}}$ in a drop-in manner using the trained decoder:

$$\mathbf{f}_{\mathbf{c}} \approx \hat{\mathbf{f}}_{\mathbf{c}} = D_\psi(\mathbf{z}, \mathbf{c}), \mathbf{z} \sim \mathcal{N}(\mathbf{0}, \mathbf{I}_d)$$

B DEEPRV HIERARCHICAL MODEL TRAINING EXAMPLE

In this section, we describe how DeepRV can be used to emulate hierarchical model directly, for example consider the following Poisson model:

$$\begin{aligned} \mathbf{c} &\sim p_{\mathcal{C}}(\cdot), \\ \mathbf{f}_{\mathbf{c}} &\sim \mathcal{GP}_{\mathbf{c}}(\cdot) \\ \beta &\sim \text{Uniform}(-3, 3) \\ \boldsymbol{\lambda} &= \exp(\beta + \mathbf{f}_{\mathbf{c}}) \\ \mathbf{y}_{\mathbf{c}} &\sim \text{Poisson}(\boldsymbol{\lambda}) \end{aligned}$$

Where $\mathbf{f}_{\mathbf{c}}$ is drawn from a Gaussian process with kernel $K_{\mathbf{c}}$. Algorithm 3, demonstrates how DeepRV can be used to directly encode the entire model, which can further accelerate inference.

Algorithm 3 Batch train step for an hierarchical Poisson model, based on a GP with kernel $k_{\mathbf{c}}(\cdot, \cdot)$

- 1: **Input:** locations \mathbf{x} , $p_{\mathcal{C}}(\cdot)$, N
 - 2: $\{(\mathbf{c}_i, \mathbf{z}_i, \beta_i)\}_{i=1}^N \leftarrow$ sample N triplets from $(p_{\mathcal{C}}(\cdot), \mathcal{N}(\mathbf{0}, \mathbf{I}_n), \text{Uniform}(-3, 3))$
 - 3: $\mathbf{L}_i = \text{Cholesky}(k_{\mathbf{c}_i}(\mathbf{x}, \mathbf{x}))$
 - 4: $\mathbf{f} \sim \text{Poisson}(\exp(\mathbf{L}_i \mathbf{z}_i + \beta_i))$
 - 5: $\hat{\mathbf{f}}_i \leftarrow \text{DeepRV}(\text{concat}(\mathbf{z}_i, \beta_i), \mathbf{c}_i)$
 - 6: $\mathcal{L} \leftarrow \frac{1}{N} \sum_{i=1}^N \text{MSE}(\mathbf{f}_i, \hat{\mathbf{f}}_i)$
 - 7: $\text{BackProp}(\mathcal{L})$
-

C PRIOR PRETRAINING

C.1 BENCHMARKING DEEPRV

Table 6: Lengthscale [5, 10]: $\text{MSE}(\mathbf{f}, \hat{\mathbf{f}})$

Spatial Prior	PriorCVAE	DeepRV + gMLP	DeepRV + MLP
Matérn 5/2	0.323 ± 0.005	0.035 ± 0.012	0.060 ± 0.001
Matérn 1/2	0.496 ± 0.002	0.007 ± 0.001	0.050 ± 0.001
Matérn 3/2	0.357 ± 0.006	0.023 ± 0.011	0.056 ± 0.001
RBF	0.267 ± 0.006	0.111 ± 0.011	0.070 ± 0.001

Table 7: Lengthscale [10, 20]: $\text{MSE}(\mathbf{f}, \hat{\mathbf{f}})$

Spatial Prior	PriorCVAE	DeepRV + gMLP	DeepRV + MLP
Matérn 5/2	0.130 ± 0.002	0.016 ± 0.004	0.025 ± 0.000
Matérn 1/2	0.308 ± 0.003	0.002 ± 0.001	0.019 ± 0.000
Matérn 3/2	0.158 ± 0.003	0.009 ± 0.003	0.028 ± 0.000
RBF	0.096 ± 0.001	0.049 ± 0.004	0.024 ± 0.000

Table 8: Lengthscale [20, 50]: $\text{MSE}(\mathbf{f}, \hat{\mathbf{f}})$

Spatial Prior	PriorCVAE	DeepRV + gMLP	DeepRV + MLP
Matérn 5/2	0.046 ± 0.000	0.008 ± 0.002	0.007 ± 0.000
Matérn 1/2	0.169 ± 0.001	0.002 ± 0.000	0.022 ± 0.000
Matérn 3/2	0.060 ± 0.001	0.005 ± 0.002	0.008 ± 0.000
RBF	0.031 ± 0.000	0.019 ± 0.001	0.006 ± 0.000

C.2 EMPIRICAL BAYES

Table 9: Empirical Bayes: MSE of ground truth vs. inferred conditional variable. The inferred variable is lengthscale for GP kernels and α for the CAR model - Eq 4.2.2.

Model	PriorCVAE	DRV + MLP	DRV + gMLP
CAR	0.00 ± 0.00	0.00 ± 0.00	0.00 ± 0.00
Matérn-1/2	0.00 ± 0.00	0.00 ± 0.00	0.00 ± 0.00
Matérn-3/2	0.00 ± 0.00	0.00 ± 0.00	0.00 ± 0.00
Matérn-5/2	0.00 ± 0.00	0.00 ± 0.00	0.00 ± 0.00
RBF	0.00 ± 0.00	0.00 ± 0.00	0.00 ± 0.00

C.3 INPUT RECONSTRUCTION FIGURES



Figure 6: Input reconstruction examples Matérn 1/2 kernel GP. 3 examples ordered by the true data f and the reconstructed data \hat{f} . Both the X and Y axes are normalized to the range $[0, 100]$.



Figure 7: Input reconstruction examples RBF kernel GP. 3 examples ordered by the true data f and the reconstructed data \hat{f} . Both the X and Y axes are normalized to the range $[0, 100]$.



Figure 8: Input reconstruction examples CAR kernel GP. 3 examples ordered by the true data f and the reconstructed data \hat{f} . Both the X and Y axes are normalized to the range $[0, 100]$.

D INFERENCE - SIMULATED DATA

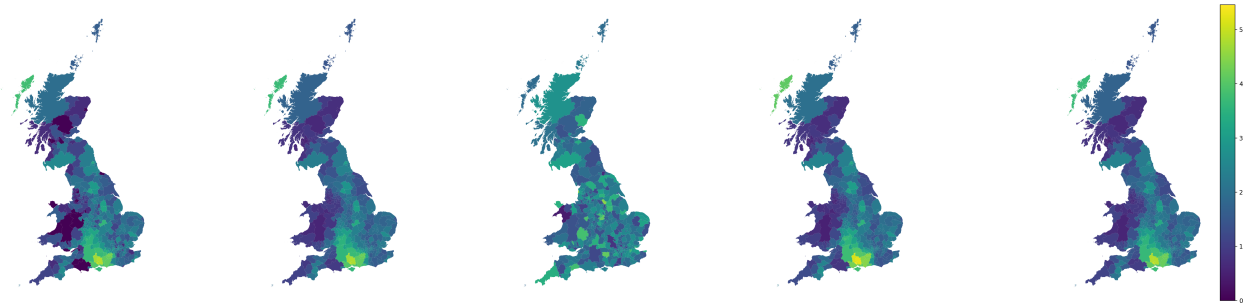


Figure 9: Simulated data posterior predictive log-scaled y means for the Matérn 1/2 kernel. (a) Observed counts, (b) GP (c) PriorCVAE, (d) DeepRV + MLP, (e) DeepRV + gMLP.

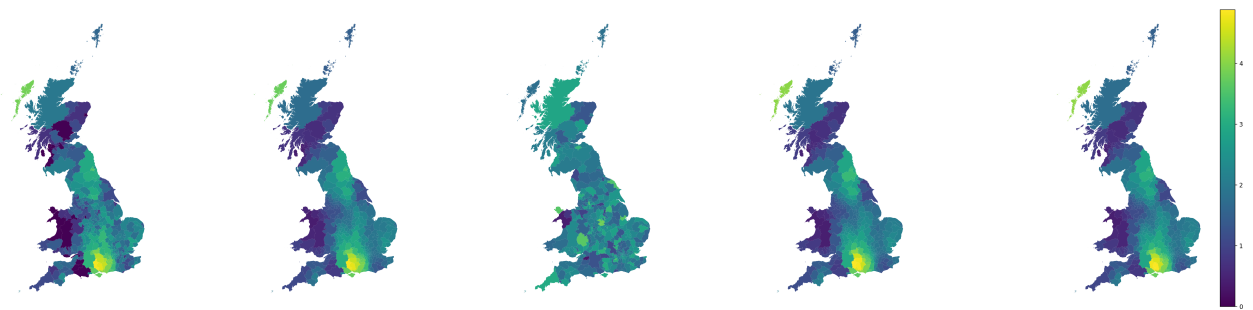


Figure 10: Simulated data posterior predictive log-scaled y means for the Matérn 3/2 kernel. (a) Observed counts, (b) GP (c) PriorCVAE, (d) DeepRV + MLP, (e) DeepRV + gMLP.

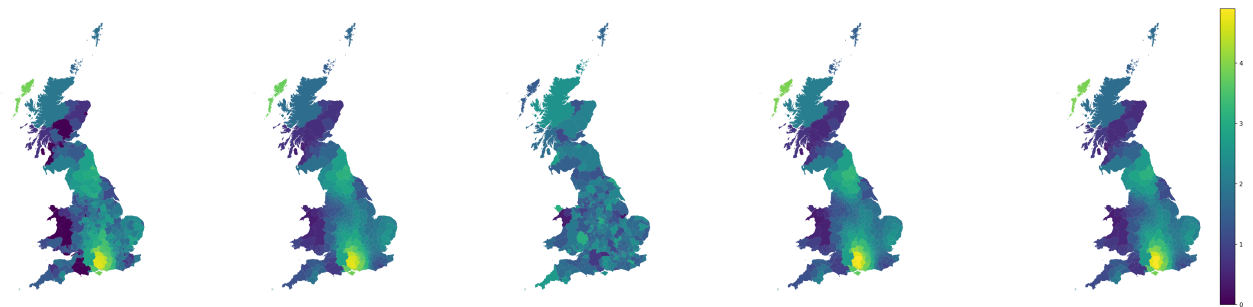


Figure 11: Simulated data posterior predictive log-scaled y means for the Matérn 5/2 kernel. (a) Observed counts, (b) GP (c) PriorCVAE, (d) DeepRV + MLP, (e) DeepRV + gMLP.

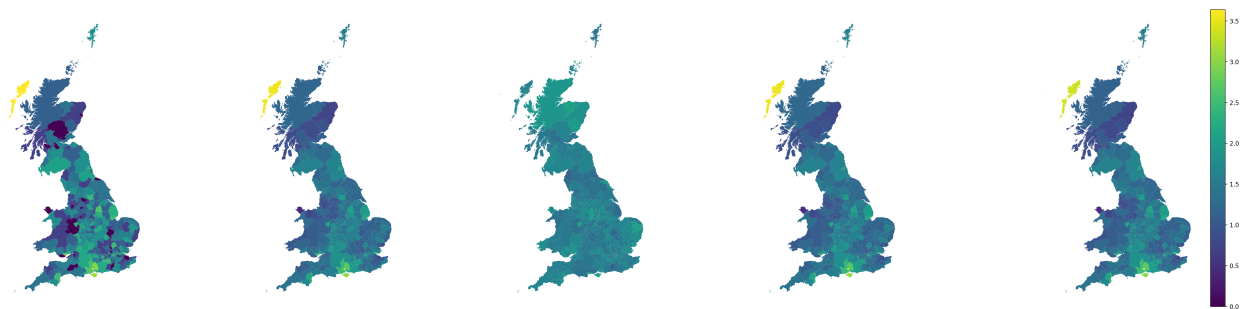


Figure 12: Simulated data posterior predictive log-scaled y means for the CAR model kernel. (a) Observed counts, (b) GP (c) PriorCVAE, (d) DeepRV + MLP, (e) DeepRV + gMLP.

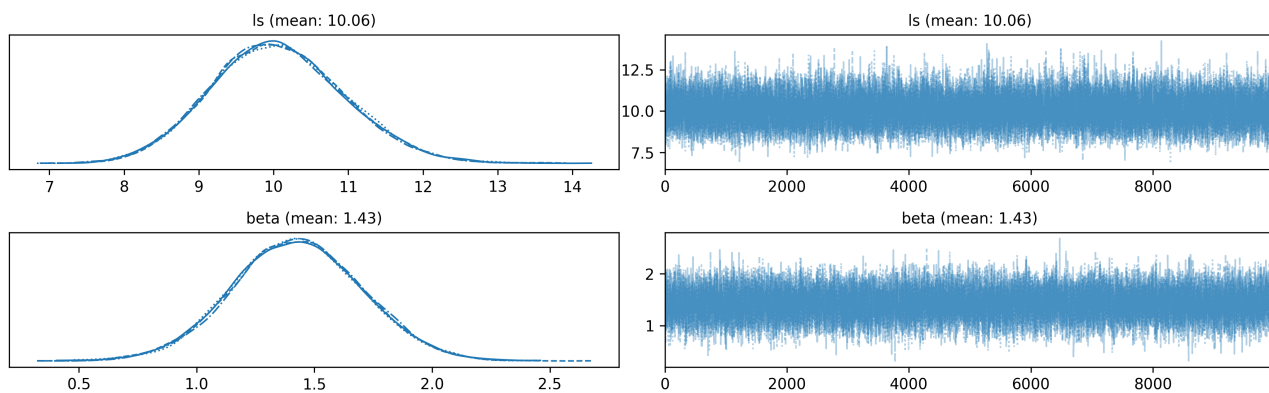


Figure 13: Full GP sampling simulated data MCMC trace plot for the Matérn 3/2 model kernel.

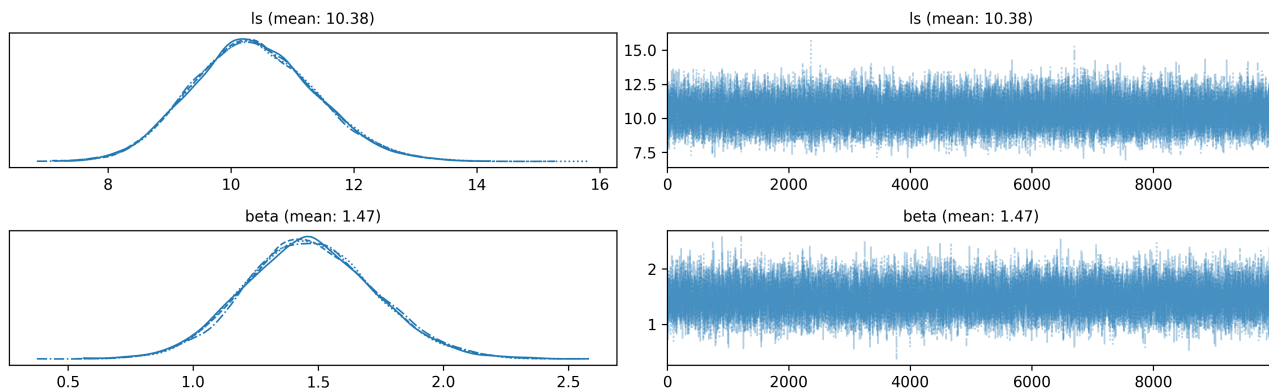


Figure 14: DeepRV + gMLP simulated data MCMC trace plot for the Matérn 3/2 model kernel

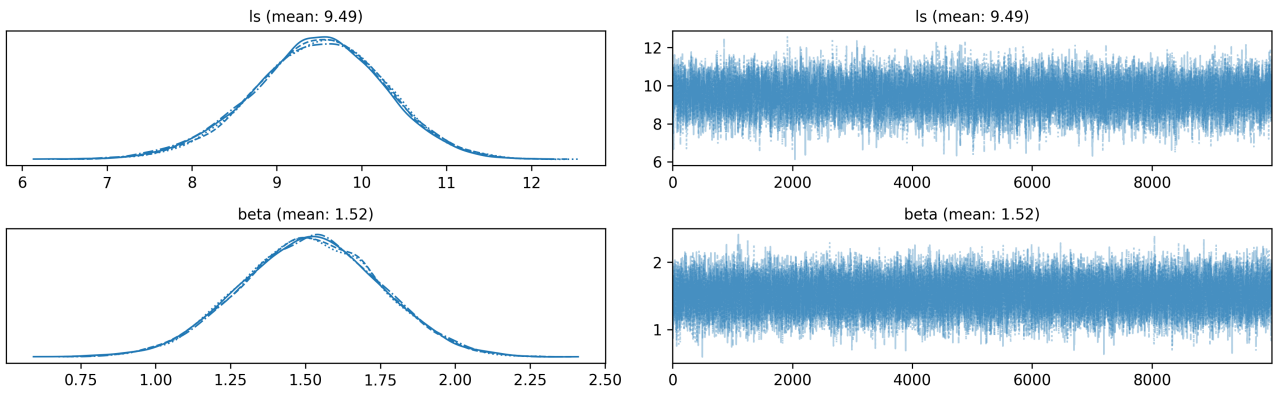
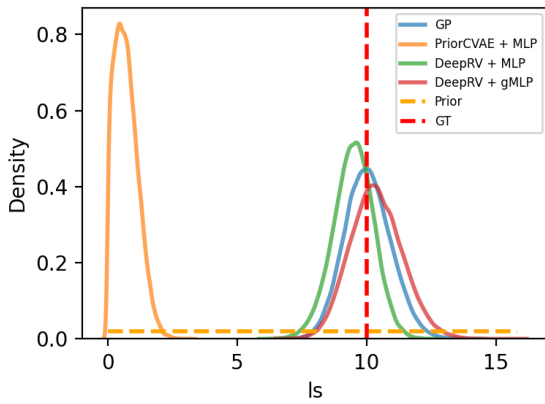
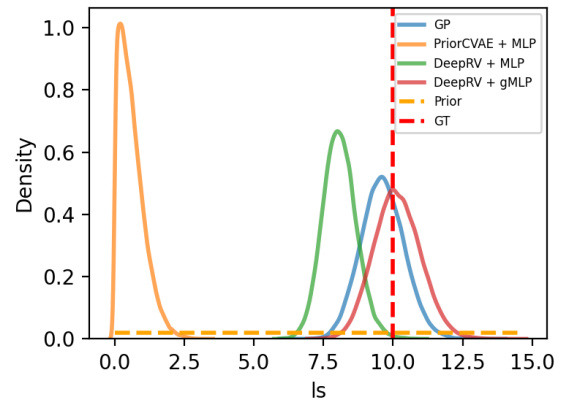


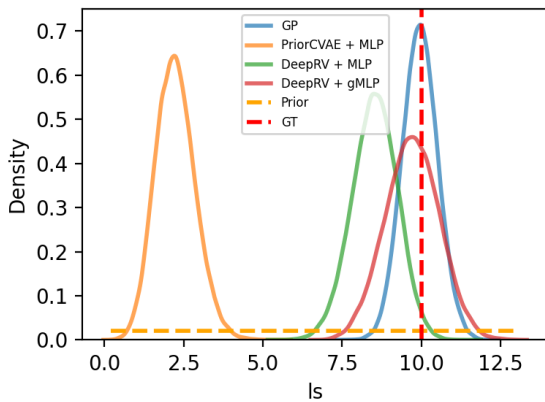
Figure 15: DeepRV + MLP simulated data MCMC trace plot for the Matérn 3/2 model kernel



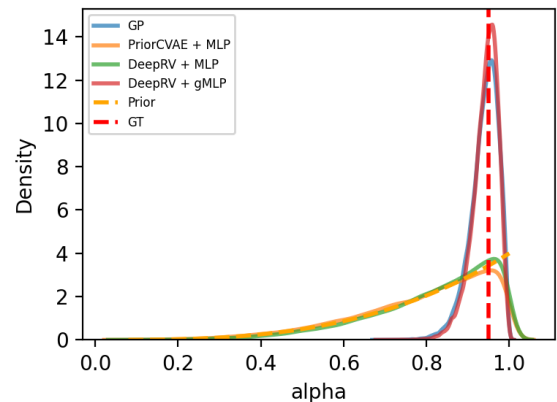
(a) Posterior predictive of lengthscale distribution for the Matérn 3/2 Kernel



(b) Posterior predictive of lengthscale distribution for the Matérn 5/2 Kernel



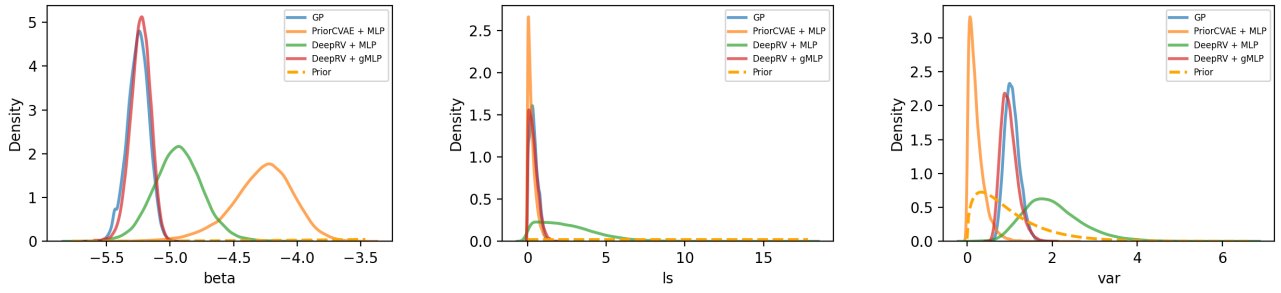
(c) Posterior predictive of lengthscale distribution for the RBF Kernel



(d) Posterior predictive of α distribution for the CAR model kernel

Figure 16: Simulated data inference for different kernels: (a) Matérn 3/2 Kernel, (b) Matérn 5/2 Kernel, (c) RBF Kernel, and (d) CAR model. The figures show the posterior predictive distributions for the respective lengthscales and α .

E INFERENCE - REAL LIFE DATA



(a) Posterior predictive of the fixed effects distribution for the Matérn 3/2 kernel

(b) Posterior predictive of the lengthscale distribution for the Matérn 3/2 kernel

(c) Posterior predictive of the variance distribution for the Matérn 3/2 kernel

Figure 17: Male under 50 cancer mortality England & Wales LAD: (a) Posterior predictive of the fixed effects distribution, (b) Posterior predictive of the lengthscale distribution, and (c) Posterior predictive of the variance distribution for the Matérn 3/2 kernel.

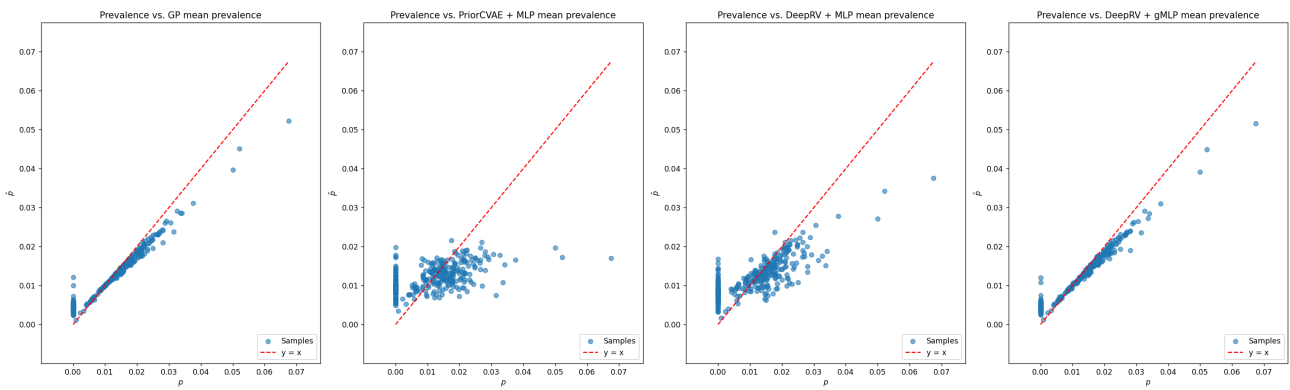


Figure 18: Female under 50 cancer mortality England & Wales LAD - prevalence p vs. mean posterior predictive prevalence \hat{p} for the Matérn-1/2 kernel.

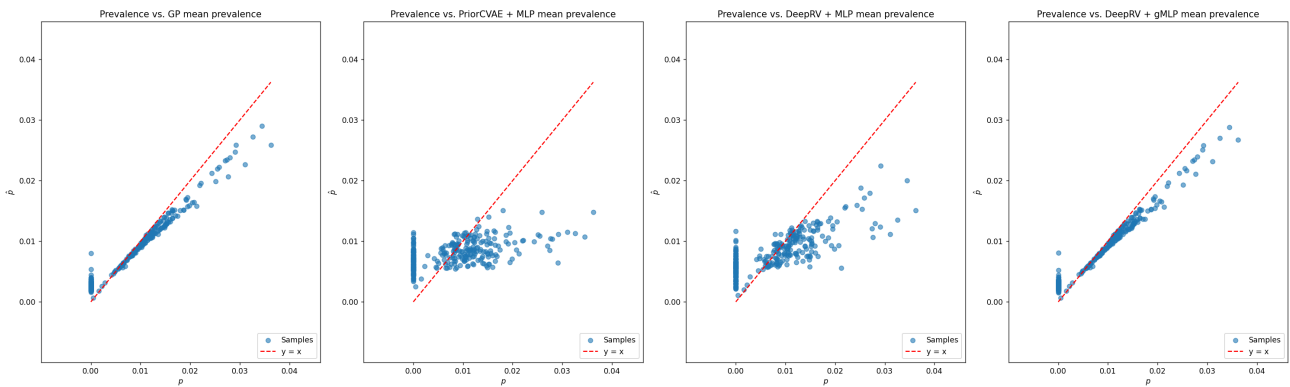
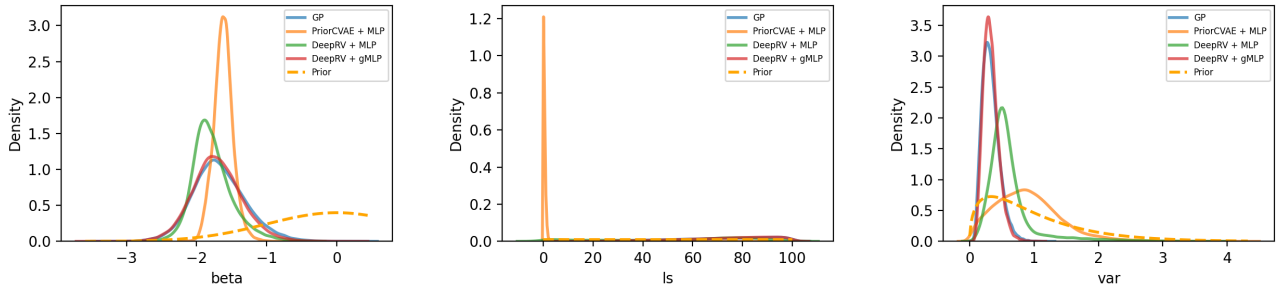


Figure 19: Male under 50 cancer mortality England & Wales LAD - prevalence p vs. mean posterior predictive prevalence \hat{p} for the Matérn-1/2 kernel.



(a) Posterior predictive of the fixed effects distribution for the Matérn 1/2 kernel (b) Posterior predictive of the lengthscale distribution for the Matérn 1/2 kernel (c) Posterior predictive of the variance distribution for the Matérn 1/2 kernel

Figure 20: Zimbabwe HIV prevalence: (a) Posterior predictive of the fixed effects distribution, (b) Posterior predictive of the lengthscale distribution, and (c) Posterior predictive of the variance distribution for the Matérn 1/2 kernel.

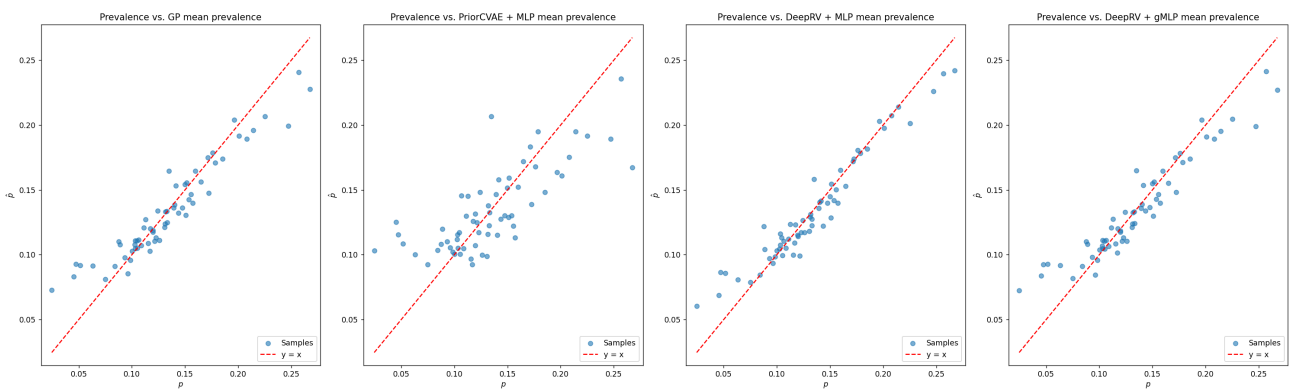


Figure 21: Zimbabwe HIV prevalence - prevalence p vs. mean posterior predictive prevalence \hat{p} for the Matérn-1/2 kernel.